2023 IEEE/ASME International Conference on Advanced Intelligent Mechatronics (AIM)
June 28-30, 2023. Seattle, Washington, USA

Modeling Solid-State LiDAR Sensor for Optimization of Area Coverage Deployment

Farsam Farzadpour, Tong Zhang, and Xiang Chen [1]

***Abstract*— This paper presents a comprehensive modeling technique for optimization of solid-state LiDAR sensor deployment. In particular, a performance measure is developed with physical parameters of flashing LiDAR sensors to describe the pose difference of the LiDAR sensor and target object. An area coverage optimization is then addressed with deployment of LiDAR sensor network (LSN) to demonstrate the effectiveness of the proposed model and the performance measure. An experiment is conducted to verify the proposed resolution criteria of the flash LiDAR sensor and simulations are carried out for validating the developed coverage model for LSN deployment.**

I. Introduction

LiDAR, an active remote-sensing system, is used in autonomous driving due to its low processing power requirements, enabling faster object detection, localization, and tracking. There is a diverse range of LiDAR sensors available in the market, which can be classified into two main categories based on their design and technology [1]: mechanical [2] and solid-state LiDAR [3], such as flash LiDAR. This paper focuses on flash LiDAR, which is widely used in various application due to the advantages like simplicity, efficiency, speed, and lower cost [4]. Its improved field of view (FOV) makes it suitable for environmental monitoring and exploration. Accurate sensor detection and data collection are crucial for achieving maximum coverage in area coverage tasks. Therefore, our study focuses on optimizing the sensor coverage model to collect more information and create a comprehensive representation of a geographic region or surface. Coverage modeling helps optimize sensor deployment based on environment, objectives, and constraints. Ray tracing is a common approach for mechanical LiDAR sensor coverage [5]. A model for 3D intersection area coverage uses integer programming [6]. Due to flash LiDAR's similarity to cameras, a camera-based model is used in [7]. A coverage model for mechanical LiDAR with rotating prisms is proposed in [8], incorporating a geometric model and sensor scanning properties. Inexpensive LiDAR sensor networks can provide high-performance sensing accuracy and precision for applications such as autonomous vehicles and robotics. However, limited research exists on LSN deployment optimization [8]. [9] explores roadside sensor placement optimization, proposing an occlusion degree model (ODM) for the 3D environment. A semi-automated framework for optimizing roadside LiDAR sensor deployment is proposed in [10], focusing on minimizing sensor count. Despite flash LSNs' potential, no research has been done on modeling their coverage or optimizing their deployment. This paper presents an approach for solid-state LiDAR sensor modeling and flash LSN deployment for area coverage tasks. The key contributions of this paper are as follows:

- A geometry model representing the effective sensing region of flash LiDAR, incorporating its physical properties, such as emitter and receiver units, and their relative configuration as concise geometry constraints.
- A performance measure to evaluate differences between LiDAR sensors and object configurations, enabling coverage model construction for flash LiDAR sensors and generic sensor network deployment for area coverage tasks [8, 11].

The paper is structured as follows: Section II explains the flash LiDAR operating principle; Section III presents the performance measure and coverage model development; Section IV covers LiDAR sensor network deployment optimization; Section V discusses simulation and experiments, and Section VI concludes.

II. Operating Principle of flash LiDAR

Flash LiDAR sensors consist of two main components: an emitter and a receiver [12]. The performance principles of the flash LiDAR are outlined as follows:

A. Field of View (FOV)

The FOV of the flash LiDAR sensor is determined by the intersection of the FOVs of both the emitter and the receiver. The emitter's field of view (FOV) is determined by the divergence angles of the laser beam, $\theta_{l,e}, \theta_{l,a} \in \left[0, \frac{\pi}{2}\right)$ (Fig. 1), and the dimension of the detector and receiving lens specify the receiver FOV which is constructed from elevation $\theta_{d,e}$ and azimuth $\theta_{d,a}$ angles (Fig. 2).

B. Resolution

The spatial resolution of the solid-state LiDAR can be divided into two main categories: axial (range or depth) resolution and lateral (cross-range) resolution.

1) Lateral resolutions: Detector lateral resolutions at depth z_r are defined by

$$R_h = \frac{2z_r \tan\left(\frac{\theta_{d,a}}{2}\right)}{w}, \tag{1}$$

$$R_v = \frac{2z_r \tan\left(\frac{\theta_{d,e}}{2}\right)}{h}, \tag{2}$$

*This work was not supported by any organization

[1]Farsam Farzadpour, Tong Zhang, and Xiang Chen are with the Department of Electrical and Computer Engineering, University of Windsor, Ontario, N9B 3P4 Canada. farzadp@uwindsor.ca, zhang14h@uwindsor.ca, xchen@uwindsor.ca

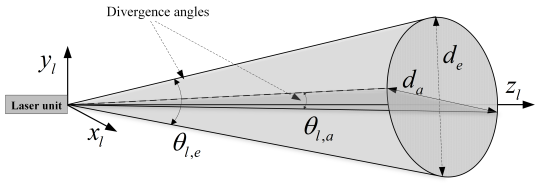

Fig. 1: Schematic diagram of the laser unit.

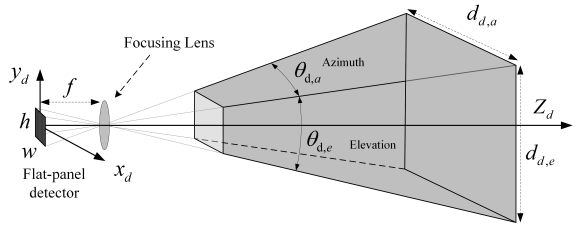

Fig. 2: Schematic diagram of the receiver unit FOV.

where $R_h, R_v \in \Re^+$ are the resolutions perpendicular to the direction of the z_d-axis along x_d and y_d, respectively. The variables w and h represent the number of vertical and horizontal pixels, respectively.

2) Depth resolution: Flash LiDAR's depth resolution along a single channel, ($R_c \in \Re^+$) depends on factors like pulse width, object size, and receiver efficiency, but this study focuses solely on pulse width's impact for a controlled analysis with minimal interference. Depth resolution is defined as:

$$R_c = \frac{cT_w}{2} = \frac{c\tau}{2}, \tag{3}$$

where $T_w \in \Re^+$ is pulse width, $c = 3 \times 10^8$m/s is the speed of light, and $\tau \in \Re^+$ is the resolution of the timer for recording pulses. That is to say, the shorter pulse width, the higher depth resolution will be.

C. Detection Range

The LiDAR detection range is calculated from the speed of light in the medium and round-trip travel time of an emitted pulse.

1) Minimum Detection Range: The minimum detection range of a LiDAR sensor depends on three factors: relative configuration of emitter and receiver (z_w), emitted pulse width (z_e), and detector saturation level (z_b). It is calculated by taking the maximum value of these factors,

$$z_{min} = \max\left(z_w, z_e, z_b\right), \tag{4}$$

where $z_w, z_e, z_b \in \Re^+$.

2) Maximum Acceptable Range: Let $R_d \in \Re^+$ be the application required resolution. The maximum acceptable range along sensor's z-axis (z_{max}) is obtained by taking the minimum of the following values:

$$z_{max} = \min\left(z_n, z_h, z_v\right), \tag{5}$$

where z_n is a nominal value specified by the sensor manufacturer and $z_h, z_v \in \Re^+$ are defined using 1 and 2 as

$$\begin{bmatrix} z_h \\ z_v \end{bmatrix} = \frac{1}{2} R_d \begin{bmatrix} \cot\left(\frac{\theta_{d,a}}{2}\right) & 1 \\ 1 & \cot\left(\frac{\theta_{d,e}}{2}\right) \end{bmatrix} \begin{bmatrix} w \\ h \end{bmatrix}, \tag{6}$$

III. Coverage Model of Flash LiDAR

A. Sensor Model

Frames F_w and F_s denote the world frame and the frame attached to the sensor, respectively, as shown in Fig. 3. The extrinsic parameters describe the sensor's 3D position in space and are defined by:

$$\mathbf{q}_s^w = \begin{bmatrix} \mathbf{r}_s & \mathbf{\Phi} \end{bmatrix}^T, \tag{7}$$

where $\mathbf{r}_s = \begin{bmatrix} x_s^w & y_s^w & z_s^w \end{bmatrix}^T$ is the position components and $\mathbf{\Phi} = \begin{bmatrix} \eta & \omega & \gamma \end{bmatrix}^T$ is the orientation components (Euler angles) with respect to F_w and obtained by rotation about X, Y and Z axis by η, ω and γ, respectively. The flash LiDAR can be modeled using the pinhole camera model due to its similarity to a camera sensor [13]. Its intrinsic parameters include focal length (f), number of pixels (W, H), pulse width (T_w), and pulse repetition frequency (PRF).

B. Environment Model

Any 3D model of the environment can be expressed to an arbitrary degree of precision by triangular mesh-based surfaces whose position and normal direction of the triangle face can be encapsulated in a vector $\mathbf{q}_t^w \in \Re^3 \times [0, \pi] \times [0, 2\pi]$, referred to as a 'task point' (Fig. 3), as

$$\mathbf{q}_t^w = \begin{bmatrix} \mathbf{r}_t & \boldsymbol{\varphi} \end{bmatrix}^T, \tag{8}$$

where $\mathbf{r}_t = \begin{bmatrix} x_t & y_t & z_t \end{bmatrix}^T$ and $\boldsymbol{\varphi} = \begin{bmatrix} \rho & \sigma \end{bmatrix}$ are the position and its directional component, respectively, defined in F_w. The superscript $(.)^w$ denotes the parameter defined in the world frame (F_w). The task point can be expressed in the sensor frame F_s, with the following relationship

$$\mathbf{q}_t^s = \left(\mathbf{R}_s^w\right)^{-1} \left(\mathbf{r}_t - \mathbf{r}_s\right), \tag{9}$$

where the superscript $(.)^s$ denotes the parameter defined in the sensor frame and $\mathbf{R}_s^w$ is the sensor rotation matrix with respect to F_w. The angle between normal direction of the triangle face ($\mathbf{n}_t$) and the opposite direction of z-axis in the sensor frame (F_s) (Fig. 3), is called (nominal) view angle and obtained by

$$\theta_t = \cos^{-1}\left(-\mathbf{n_s} \cdot \mathbf{n_t}\right), \tag{10}$$

where $\mathbf{n_s}$ and $\mathbf{n_t}$ are unit vectors, defined as follows:

$$\mathbf{n_s} = \mathbf{R}_s^w \mathbf{J}, \tag{11}$$

where $\mathbf{J} = \begin{bmatrix} 0 & 0 & 1 \end{bmatrix}^T$, and

$$\mathbf{n_t} = \begin{bmatrix} \sin(\rho)\cos(\sigma) & \sin(\rho)\sin(\sigma) & \cos(\rho) \end{bmatrix}^T \tag{12}$$

where ρ and σ are shown in Fig. 3.

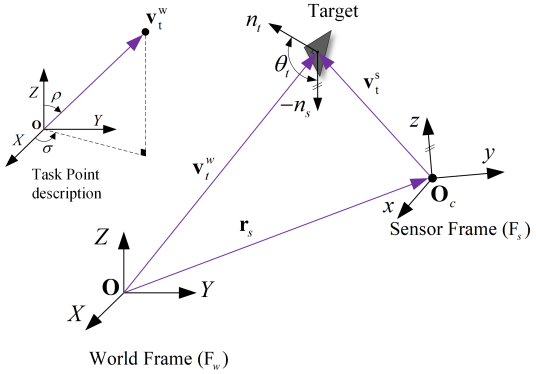

Fig. 3: World and sensor coordinate systems description.

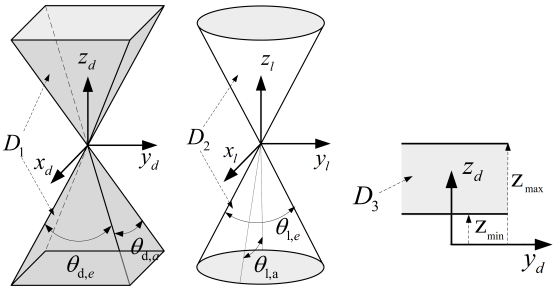

(a) F_1. (b) F_2. (c) F_3, F_4.

Fig. 4: Geometric modeling of effective sensing region.

C. Geometric Model

This section presents a method to construct the geometric model of a LiDAR sensor's sensing region (D) in 3D space. The sensing region can be regular or irregular, depending on the relative configuration of the emitter and receiver [1]. The visibility region is shaped like a pyramid based on the receiver's field of view. The region is bounded by an implicit surface function, denoted by $D_1 \subset \Re^3$ and shown in Fig. 4a, given by

$$F_1(x_d, y_d, z_d) = \max\left(\frac{{x_d}^2}{tan^2\left(\theta_{d,a}/2\right)}, \frac{{y_d}^2}{tan^2\left(\theta_{d,e}/2\right)}\right) - {z_d}^2, \tag{13}$$

The intersection of multiple convex regions is a convex region, implying that D_E, the intersection of D_1, D_2, and D_3 in $\Re^3$, is also convex. Moreover, D_E is radially convex with respect to any point $\mathbf{O}_c \in D_E$ due to its convexity [14, 15].

$$F_2(x_l, y_l, z_l) = \frac{{x_l}^2}{tan^2\left(\theta_{l,a}/2\right)} + \frac{{y_l}^2}{tan^2\left(\theta_{l,e}/2\right)} - {z_l}^2\,. \tag{14}$$

Considering the LiDAR detection range, we have

$$z_{\min} \leq z_d \leq z_{\max} \tag{15}$$

Thus, the implicit equation of a planes pass through $z_d = z_{min}$ and $z_d = z_{max}$ are defined as

$$F_3 = z_d - z_{\min}, \tag{16}$$

$$F_4 = z_d - z_{\max}, \tag{17}$$

Let $D_3 \subset \Re^3$ denote the region between these two planes. Therefore, the effective sensing region (D_E) of the flash LiDAR (Fig. 5) is determined by

$$D_E = \bigcap_{i=1}^{3} D_i\,. \tag{18}$$

The intersection of convex regions D_1, D_2, and D_3 in $\Re^3$ is convex, so D_E is also convex. D_E is radially convex with respect to any point $\mathbf{O}_c \in D_E$ [14].

D. Performance Measure

The parametric equation of the ray starting at the origin $\mathbf{O}_c$ toward the given point $\mathbf{p_t} \in \Re^3$ (Fig. 5) is given by

$$\mathbf{P}(l) = \mathbf{O}_c + l\mathbf{v}\,, \tag{19}$$

where the unit vector $\mathbf{v}$ is defined as

$$\mathbf{v} = \begin{cases} \frac{\mathbf{p_t} - \mathbf{O}_c}{\|\mathbf{p_t} - \mathbf{O}_c\|} & for\ \mathbf{p_t} \in \Re^3 - \{\mathbf{O}_c\} \\ 0 & for\ \mathbf{p_t} = \mathbf{O}_c \end{cases}, \tag{20}$$

where $\|\cdot\|$ denotes the Euclidean norm and $l \in \Re^+$ is the distance along the ray from origin $\mathbf{O_c}$. The set $D_E \subseteq \mathbb{R}^3$ can be described as a radially convex entity with respect to the origin $\mathbf{O}_c$, and its sensing region $\partial D_E \subseteq \mathbb{R}^2$ is bounded by a surface (Fig. 5). Based on these constraints, the following proposition can be deduced:

Let $F(\mathbf{X}) = 0$ for $\mathbf{X} \in \Re^3$ be the system of equations representing the implicit function of the region boundary (∂D_E) defined in F_s and let M denote the set of all solutions to $F(\mathbf{P}(\alpha)) = 0$ for $\alpha \geqslant 0$. Then, the intersection point $\mathbf{P}(l_i)$ of the ray $\mathbf{P}(l)$ and the boundary ∂D_E is determined by

$$\mathbf{P}(l_i) = \mathbf{O}_c + l_i\mathbf{v}, \tag{21}$$

where $l_i \leq l_t$ is the distance along the ray between point $\mathbf{O_c}$ and $\mathbf{p_t}$ as depicted in Fig.5. Thus, given the intersection point of the ray $\mathbf{P}(l)$ with the origin at $\mathbf{O_c}$ and the boundary ∂D_E, the radial projection $H : \partial D_E \rightarrow \mathbb{S}^2(R)$ is defined by

$$H\left(\mathbf{p}_t\right) = \mathbf{p}_t \frac{R}{\|\mathbf{P}(l_i)\|}\ ;\ \forall \mathbf{p}_t \in D, \mathbf{P}(l_i) \in \partial D, \tag{22}$$

where $\mathbb{S}^2(R)$ is the sphere of radius R in 3-dimensional space. Therefore, having the sensor's sensing region transformed into a closed ball ($\mathbb{B}^3$), the proximity of a task point ($\mathbf{q}_t^s$) with respect to the center of $\mathbb{S}^2(R)$ is defined by

$$\Gamma(\mathbf{q}_t^s) = \frac{\|H\left(\mathbf{p}_t^s\right)\|}{R}. \tag{23}$$

Thus, an equivalent form in the Euclidean space (original domain) is defined as

$$\Gamma(\mathbf{q}_t^s) = \frac{\|\mathbf{r}\left(l\right)\|}{\|\mathbf{r}\left(l_i\right)\|}. \tag{24}$$

The degree of alignment between a $\mathbf{q}_t^s$ and the sensor frame can be determined by defining a non-negative function Ψ :

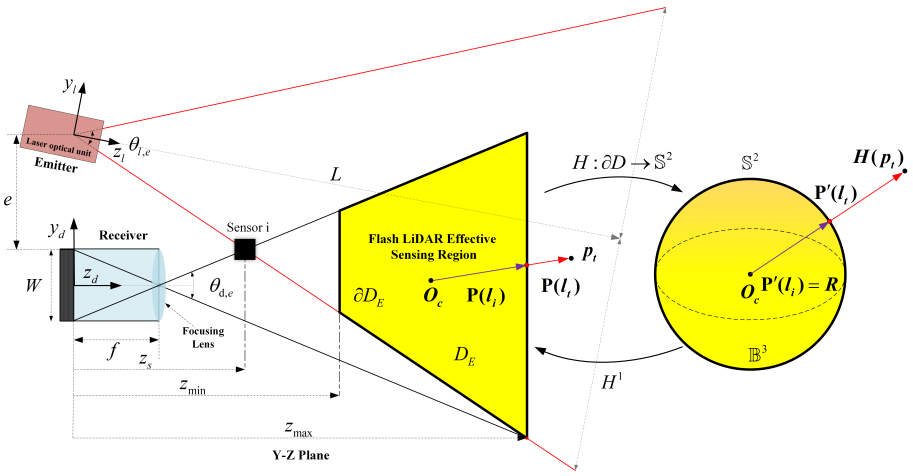

Fig. 5: Overlooking schematic of bi-static configuration of the receiver and emitter and mapping D_E to the $\mathbb{B}^3$.

$[0,\pi] \to [0,\infty)$ as

$$\Psi(\boldsymbol{\varphi}) = \frac{\tan(\theta_t/2)}{\tan(\theta_a/2)}, \tag{25}$$

where $\theta_a \in [0,\pi]$ is the application dependent acceptable view angle defined by end-user. Thus, a performance measure can be defined by considering both the position and orientation of the task point with respect to the sensor as

$$d_s(\mathbf{q}_s^w, \mathbf{q}_t^s) = \left\| \begin{bmatrix} \Gamma & \Psi & \Delta(\Gamma+\Psi) \end{bmatrix}^T \right\|_F, \tag{26}$$

where $d_s : \Re^3 \times [0,\pi] \times [0,2\pi] \to \Re^+$ is a monotonic function [1], $\|\cdot\|_F$ is the Frobenius norm, and Δ is defined as

$$\Delta = \lfloor \max(\Gamma, \Psi) \rfloor^+, \tag{27}$$

where $\lfloor A \rfloor^+$ denotes the largest integer smaller than A.

E. Single Sensor Coverage

According to Theorem 3.2 in [1], a task point is covered if it falls inside or on the boundary of the sensor's sensing region D_E or the mapped region $\mathbb{B}^3$ and satisfies the view angle criterion ($\theta_t \leq \theta_a$). The coverage model for a LiDAR sensor with respect to a single task point is defined as

$$C(\mathbf{q}_s^w, \mathbf{q}_t^s) = e^{-\mu d_s(\mathbf{q}_s^w, \mathbf{q}_t^s)}, \tag{28}$$

where $\mu \in \Re^+$ is the decaying rate constant which reflects physical characteristics of the space.

F. Sensor Network Coverage

Let $\mathbb{T}$ be a set of task points representing the 3D environment model and $\mathbf{Q}(t) = \{\mathbf{q}_{s,1}^w(t), \mathbf{q}_{s,2}^w(t), ..., \mathbf{q}_{s,n}^w(t)\}$ be the configuration of n sensors at time t, the overall coverage performance function of the sensor network is given by

$$\mathcal{H}(\mathbf{Q}) = \int_{\mathbb{T}} \max_{i \in s_n} \{C_i(\mathbf{q}_{s,i}^w, \mathbf{q}_t^s)\} \phi(\mathbf{q}_t^s)\, d\mathbb{T}, \tag{29}$$

where $s_n = \{1, ..., n\}$ is the list of deployed sensors and $\phi(\mathbf{q}_t^s) \in [0,1]$ is the relevance function which is a measure of relative importance of task points $\mathbf{q}_t^s$ [3].

IV. Optimized Sensor Network Deployment

Proposed framework for optimized sensor network deployment includes gradient-based optimization and modified Voronoi partitioning.

A. Environment partitioning

We propose a novel non-Euclidean Voronoi partitioning based on an advanced performance measure as detailed below:

$$V_i = \{\mathbf{q}_t^s \in \mathbb{T} | d_s(\mathbf{q}_{s,i}^w, \mathbf{q}_t^s) \leq d_s(\mathbf{q}_{s,j}^w, \mathbf{q}_t^s), \forall j \neq i, j \in s_n\} \tag{30}$$

where V_i is the Voronoi partition associated with i-th sensor. Thus, (29) can be rewritten as

$$\mathcal{H}(\mathbf{Q}) = \sum_{i \in s_n} \int_{\mathbf{q}_t^s \in V_i} C_i(\mathbf{q}_{s,i}^w, \mathbf{q}_t^s) \phi(\mathbf{q}_t^s)\, d\mathbf{q}_t^s. \tag{31}$$

B. Control Law

Optimizing sensor network coverage for area tasks can be achieved by maximizing the performance function $\mathcal{H}$ using a gradient-based optimization approach and first-order system dynamics for the control law.

$$\dot{\mathbf{q}}_{s,i}^w(t) = \mathbf{u}_i(t), \tag{32}$$

for $i \in s_n$ and

$$\mathbf{u}_i(t) = \begin{bmatrix} \mathbf{w}_i & \boldsymbol{\tau}_i \end{bmatrix}^T = \begin{bmatrix} K_x \dfrac{\partial \mathcal{H}}{\partial \mathbf{r}_{s,i}(t)} & K_{\boldsymbol{\varphi}} \dfrac{\partial \mathcal{H}}{\partial \Phi_i(t)} \end{bmatrix}^T, \tag{33}$$

where $\mathbf{w}_i$ and $\boldsymbol{\tau}_i$ are the sensor's linear and angular velocity, respectively. The control law guides the sensors towards the gradient direction using constant step sizes K_x and $K_{\boldsymbol{\varphi}}$, subject to maximum speed constraints on the linear and angular speed, denoted as $\mathbf{w}_{i,\max}$ and $\tau_{i,\max}$ respectively. The constrained control law can be expressed as:

$$\boldsymbol{u}_i^c = \begin{bmatrix} \mathbf{w}_i^c & \boldsymbol{\tau}_i^c \end{bmatrix}^T, \tag{34}$$

where

$$\mathbf{w}_i^c = \begin{cases} \mathbf{w}_i & \|\mathbf{w}_i\| \leqslant \mathbf{w}_{i,\max} \\ \mathbf{w}_{i,\max} \frac{\mathbf{w}_i}{\|\mathbf{w}_i\|} & otherwise \end{cases}, \tag{35}$$

TABLE I: LiDAR $VU8$ specifications for experiments.

Parameters	Variable	Value
Pulse width	T_ω	20 ns
Azimuth angle	$\theta_{d,a}$	$92^\circ \pm 4^\circ$
Elevation angle	$\theta_{d,e}$	$3^\circ \pm 0.6^\circ$
Detector width	w	8 channels
Detector height	h	1 channel

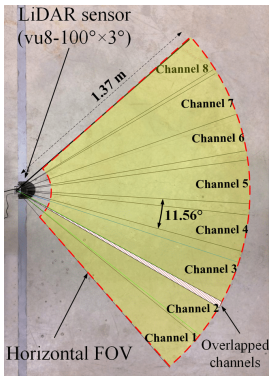

Fig. 6: Horizontal resolution validation experiment setup.

$$\boldsymbol{\tau}_i^c = \begin{cases} \boldsymbol{\tau}_i & \|\boldsymbol{\tau}_i\| \leq \boldsymbol{\tau}_{i,\max} \\ \boldsymbol{\tau}_{i,\max}\text{sgn}(\boldsymbol{\tau}_i) & otherwise \end{cases} . \tag{36}$$

The sensors' trajectories, governed by the proposed control laws, will converge to a local minimum of $\mathcal{H}$ (i.e., configurations where $\frac{\partial \mathcal{H}}{\partial \mathbf{q}s,i^w}$ is zero) with any initial configuration and an appropriate constant step size [16]. The performance function $d_s\left(\mathbf{q}s, i^w, \mathbf{q}_t^s\right)$ can be redefined as:

$$d_s\left(\mathbf{q}_{s,i}^w, \mathbf{q}_t^s\right) = \begin{cases} \Upsilon_1 & for\ \Delta = 0 \\ \Upsilon_2 & for\ \Delta \neq 0 \end{cases} , \tag{37}$$

Thus, V_i can be divided into two disjoint sub-partitions, $V_i = V_i^1 \cup V_i^2$ such that

$$V_i^1 = \left\{\mathbf{q}_t^s \in \mathbb{T} | d_s\left(\mathbf{q}_{s,i}^w, \mathbf{q}_t^s\right) = \Upsilon_1\right\} , \tag{38}$$

and

$$V_i^2 = \left\{\mathbf{q}_t^s \in \mathbb{T} | d_s\left(\mathbf{q}_{s,i}^w, \mathbf{q}_t^s\right) = \Upsilon_2\right\} . \tag{39}$$

by considering sub-partitions of V_i, we have

$$\frac{\partial \mathcal{H}}{\partial \mathbf{q}_{s,i}^w} = \int_{V_i^1} \frac{\partial}{\partial \mathbf{q}_{s,i}^w}\left(e^{-\mu_d \Upsilon_1}\right)\phi\left(\mathbf{q}_t^s\right) d\mathbb{T} + \int_{V_i^2} \frac{\partial}{\partial \mathbf{q}_{s,i}^w}\left(e^{-\mu_d \Upsilon_2}\right)\phi\left(\mathbf{q}_t^s\right) d\mathbb{T} . \tag{40}$$

V. Simulation and Experimental Verification

A. Experiments

We experimentally validated the Flash LiDAR resolution criteria using a $VU8 - 100^\circ \times 3^\circ$ LiDAR sensor with 10 cm distance accuracy. The sensor's theoretical Eq.(1) horizontal resolution is $R_{h,T} = 0.34\ m$, while the measured horizontal resolution from experiments is $R_{h,E} = 0.36\ m$ (Fig. 6). The sensor's vertical resolution is theoretically $R_v = 0.072\ m$ Eq.(2) and experimentally measured as $R_{v,E} = 0.065\ m$ (Fig. 7). The experiments used a $15 \times 20 \times 60\ cm$ object.

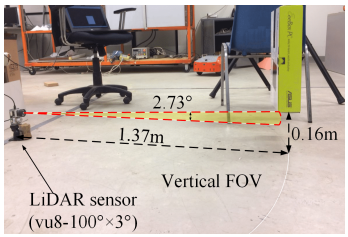

Fig. 7: Experimental setup for vertical resolution validation.

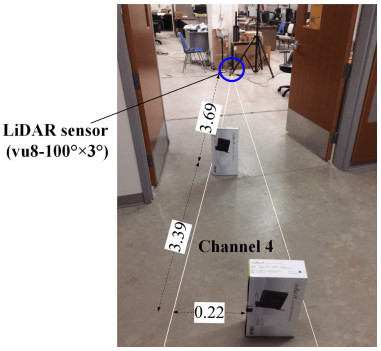

Fig. 8: Experimental set up for depth resolution validation.

Depth Resolution Validation

Flash LiDAR's 20 ns pulse width achieves a $R_c = 3\ m$ depth resolution per channel (Eq. 3) and is experimentally confirmed with a minimum detectable distance of 3.39 m (Fig. 8). See Table II for results and errors.

B. Simulation

Simulation carried out for LSN deployment optimization for area coverage task with $n = 7$ sensors, initial random configuration, and a conical frustum sensing region geometry (Fig. 9). Decaying rate for all sensors selected as $\mu = 0.01$ and relevance function $\phi\left(\mathbf{q}t^s\right) = 1$. Gradient-based control law with proportional constants $K_x = 0.5$ and $K\phi = 1.0e-05$ and step size of 0.1. Maximum linear and angular speeds selected as 0.05 m/s and 0.005 rad/s, respectively. Sensors were guided by the performance function's gradient direction and spread over the entire area after 90 seconds, as depicted in Fig. 10. Fig. 11 illustrates the coverage performance during optimization, showing a gradual increase in overlap and $\mathcal{H}$ under the proposed control law, with stability reached after 90 seconds and convergence to a critical point of $\mathcal{H}$.

VI. Conclusion

This paper presents a coverage model and optimization framework for sensor network deployment tailored to solid-state LiDAR sensors. The flash LiDAR operating principle is researched and resolution criteria are identified and tested through experimental evaluations. A simulation validates the efficacy of the proposed optimization approach for flash LSNs in 3D space. Future work should investigate laser emitter properties to improve the LiDAR coverage model's

TABLE II: Resolution validation results at $z_r = 1.37\ m$.

Parameters	Theoretical [m]	Experimental [m]	Error [m]
Horizontal Resolution (R_h)	0.34	0.36	0.02
Vertical Resolution (R_v)	0.072	0.065	0.007
Depth Resolution (R_d)	3.0	3.39	0.39

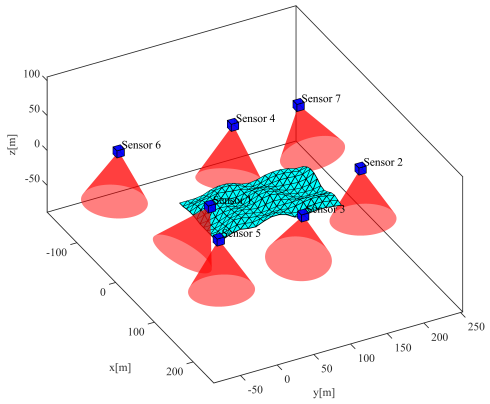

Fig. 9: Random LiDAR network deployment.

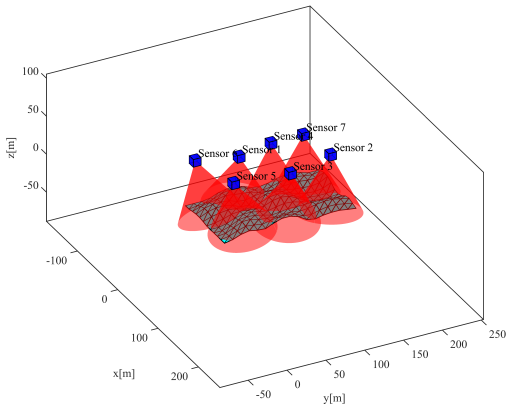

Fig. 10: Optimized configuration for surface coverage.

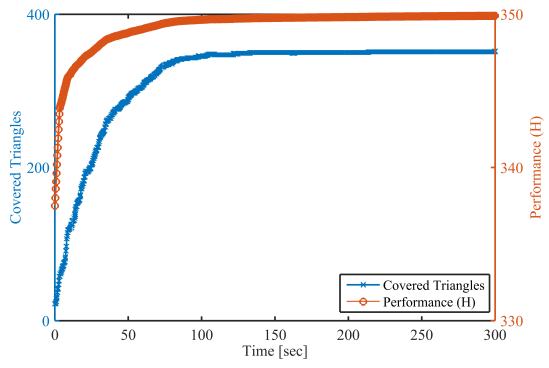

Fig. 11: LSN optimization performance over time.

accuracy. Additionally, exploring the impact of environmental factors such as foggy conditions and glass reflectivity can further improve the performance of cost-effective flash LiDAR sensor networks in autonomous driving and virtual testing applications.

REFERENCES

[1] F. Farzadpour, "A new measure for optimization of field sensor network with application to lidar," Ph.D., University of Windsor, Windsor, ON, 2018.

[2] C. Toth, G. Jozkowa, Z. Koppanyi, S. Young, and D. Grejner-Brzezinska, "Monitoring aircraft motion at airports by lidar." *ISPRS Annals of Photogrammetry, Remote Sensing & Spatial Information Sciences*, vol. 3, no. 1, 2016.

[3] F. Farzadpour, X. Zhang, X. Chen, and T. Zhang, "On performance measurement for a heterogeneous planar field sensor network," in *2017 IEEE International Conference on Advanced Intelligent Mechatronics (AIM)*. IEEE, 2017, pp. 166–171.

[4] C. Mallet and F. Bretar, "Full-waveform topographic lidar: State-of-the-art," *ISPRS Journal of photogrammetry and remote sensing*, vol. 64, no. 1, pp. 1–16, 2009.

[5] A. Haider, M. Pigniczki, M. H. Köhler, M. Fink, M. Schardt, Y. Cichy, T. Zeh, L. Haas, T. Poguntke, M. Jakobi *et al.*, "Development of high-fidelity automotive lidar sensor model with standardized interfaces," *Sensors*, vol. 22, no. 19, p. 7556, 2022.

[6] R. Vijay, J. Cherian, R. Riah, N. De Boer, and A. Choudhury, "Optimal placement of roadside infrastructure sensors towards safer autonomous vehicle deployments," in *2021 IEEE International Intelligent Transportation Systems Conference (ITSC)*. IEEE, 2021, pp. 2589–2595.

[7] M. Kettelgerdes and G. Elger, "Modeling methodology and in-field measurement setup to develop empiric weather models for solid-state lidar sensors," *IEEE Journal of Radio Frequency Identification*, 2023.

[8] F. Farzadpour, P. Church, and X. Chen, "Modeling and optimizing the coverage performance of the lidar sensor network," in *2018 IEEE/ASME International Conference on Advanced Intelligent Mechatronics (AIM)*. IEEE, 2018, pp. 504–509.

[9] Y. Du, F. Wang, C. Zhao, Y. Zhu, and Y. Ji, "Quantifying the performance and optimizing the placement of roadside sensors for cooperative vehicle-infrastructure systems," *IET Intelligent Transport Systems*, vol. 16, no. 7, pp. 908–925, 2022.

[10] Y. Ma, Y. Zheng, S. Wang, Y. D. Wong, and S. M. Easa, "Point cloud-based optimization of roadside lidar placement at constructed highways," *Automation in Construction*, vol. 144, p. 104629, 2022.

[11] X. Zhang, X. Chen, F. Farzadpour, and Y. Fang, "A visual distance approach for multicamera deployment with coverage optimization," *IEEE/ASME Transactions on Mechatronics*, vol. 23, no. 3, pp. 1007–1018, 2018.

[12] P. Meszmer, N. Mundada, M. Tavakolibasti, and B. Wunderle, "Ai surrogate models for error analysis in optical systems," in *2023 24th International Conference on Thermal, Mechanical and Multi-Physics Simulation and Experiments in Microelectronics and Microsystems (EuroSimE)*. IEEE, 2023, pp. 1–9.

[13] C. Jang, C. Kim, K. Jo, and M. Sunwoo, "Design factor optimization of 3d flash lidar sensor based on geometrical model for automated vehicle and advanced driver assistance system applications," *International journal of automotive technology*, vol. 18, pp. 147–156, 2017.

[14] Y. Nakamura, "Characterization of convexity of intersection of sets," *arXiv preprint arXiv:1909.04983*, 2019.

[15] H. Brezis, *Convex Analysis and Monotone Operator Theory in Hilbert Spaces*. Springer, 2010.

[16] K. Guruprasad and D. Ghose, "Heterogeneous locational optimisation using a generalised voronoi partition," *International Journal of Control*, vol. 86, no. 6, pp. 977–993, 2013.